JOURNAL OF MATERIALS SCIENCE 32 (1997) 4875–4887

Transformation toughening in the γ-TiAl–β-Ti–V system

Part II *A molecular dynamics study*

P. DANG, M. GRUJICIC
Program in Materials Science and Engineering, Department of Mechanical Engineering, 241 Flour Daniel Building, Clemson University, Clemson, SC 29634–0921, USA

Molecular dynamics simulations of the evolution of materials in a region surrounding a crack tip were carried out for the case of a crack in a γ-TiAl phase impinging at a right angle onto the interface between a γ-TiAl phase and a metastable Ti–15V (at %) phase. The corresponding linear anisotropic solutions for the singular stress and displacement fields were used to both generate the crack in the original crystal and to prescribe the boundary conditions applied to the computational crystal during the molecular dynamics simulation runs. The atomic interactions were accounted for using appropriated embedded atom method (EAM) type interatomic potentials. The crack-tip behaviour for the two-phase γ–β material was ultimately compared with the one in the corresponding single-phase material, i.e. to the one in pure γ and the one in pure β crystals. The simulation results showed that under the same applied level of external stress, the crack tip became blunt and the crack stopped propagating in the γ-TiAl–β-Ti–15V bicrystal and in the single β-phase crystal while the crack extended by brittle cleavage in the single-phase γ crystal. The blunting process was found to be controlled by the martensitic transformation that took place in the β-phase ahead of the crack tip. Depending on the local stress conditions the crystal structure of martensite was found to be either hexagonal close packed (h.c.p.), body centred orthorhombic (b.c.o.) and/or face centred orthorhombic (f.c.o.). Finally the implications of crack tip martensitic transformation on the toughness of the materials are analysed in quantitative terms using the concept of Eshelby's conservation integral, i.e. the energy release rate.

1. Introduction

The occurrence of stress–strain-induced martensitic transformation in materials ahead of propagating cracks has resulted in record fracture toughness levels both in metals [1] and ceramics [2]. In our ongoing research we have recently found a two-fold increase in room temperature fracture toughness of single-phase γ-TiAl when 10 vol % of a metastable dispersed Ti–V β-phase is added that undergoes stress–strain induced body centred cubic (b.c.c.) → orthorhombic martensitic transformation [3]. Because limited fracture toughness and tensile ductility at temperatures below ~600 °C are the major obstacles to wide-scale application of γ-TiAl, transformation toughening appears to have potential in resolving this problem.

Modelling of the evolution of materials in a region surrounding a crack tip and the associated mechanism of transformation toughening have been generally carried out using the continuum material approach in which no account of the microstructure of the material is made [4]. While such an approach is very useful in identifying more macroscopic aspects of the underlying process, the small-scale (e.g. atomic-scale) events that control the crack-tip blunting process, and hence play a very important role in the fracture process, are neglected. This may be one of the reasons why the continuum approach can typically account for only about half of the observed increase in fracture toughness [5]. Because atomic-scale events are difficult to study experimentally, their effect on fracture toughness cannot be measured easily. Fortunately, recent advances in computational materials science coupled with higher affordability of the more powerful (higher speed–larger memory) computers have enabled atomistic computer modelling of crack-tip phenomena to become a respectable alternative for elucidating the role of small-scale effects on the fracture process.

Among various atomistic modelling techniques, molecular dynamics is particularly attractive because it enables time evolution of the material around the crack tip, including crack-tip phase transformation, to be studied. For example, Hoagland *et al.* [6, 7] used molecular dynamics simulations to analyse dislocation emission from the crack tip, which resulted in crack-tip blunting and, in turn, enhanced the toughness of the material. Clapp and coworkers [8–11] carried out an extensive molecular dynamics study of the thermally-induced and stress-assisted B2 → $L1_0$ martensitic transformation in ordered NiAl, while Williaime and Massobio [12] carried out a similar

0022–2461

study for the b.c.c → h.c.p. transformation in Zr. Recently, Grujicic and Dang [13–15] conducted a thorough molecular dynamics investigation of the face centred cubic (f.c.c.) → b.c.c. martensitic transformation in Fe–(20–40)Ni (at %), and of the b.c.c. → h.c.p. transformation in Ti–(0–25) V (at %). These investigations were subsequently extended to include cases where the aforementioned phase transformations took place in the region around the crack tip and became the dominant crack-tip blunting, i.e. toughening, mechanism [16, 17].

In each of the molecular dynamics studies mentioned above, starting atomic configurations corresponding to a single-phase material were used. The work presented in this paper, on the other hand, deals with the a two-phase material, in which one phase, γ-TiAl, contains a crack; while the other phase, β-Ti–V, is metastable and can undergo a stress–strain-induced martensitic transformation. To simplify the analysis, the following assumptions are made in the present work: (a) the γ–β interface is planar, (b) the crack plane is normal to the interface plane and (c) the crack either touches the interface or is only a few atomic spacings away from it. To carry out molecular dynamics atomistic simulations of the crack-tip phenomena in the two-phase γ–β material described above, linear elastic continuum solutions for the corresponding stress and displacement fields must be available so that more realistic boundary conditions can be imposed on the atomistic computational crystal used in the simulations. These linear elastic solutions have been derived in Part I of this paper [18], and will be used here.

The organization of the present paper is as follows: the embedded atom method (EAM) interatomic potentials used to describe atomic interactions are briefly discussed in Section 2. The procedures used to generate and equilibrate the two-phase (γ + β) atomistic computational bicrystal and to introduce a crack in the γ-phase are described in Section 2. A brief account of the molecular dynamics computational method used is given in Section 2. In Section 3, the results are presented and discussed. The main conclusions resulting from the present work are listed in Section 4.

2. Computational procedure

2.1. Interatomic potentials

The interatomic potentials that account for atomic interactions in the crystal are the required input for the atomistic simulations and therefore their reliability and accuracy are critical for the atomistic simulations to be able to represent the behaviour of the material faithfully. In contrast to traditional pair potentials, (EAM) interatomic potentials take into account in an implicit way the many-body effects and have therefore been proven more reliable in representing atomic interactions in metals [19, 20]. Within the EAM scheme the total potential energy of the system is given as the sum of two terms: (a) the interaction of each atom with the local electron density associated with the remaining atoms in the system, called the embedding energy; and (b) a pairlike interaction reflecting the electrostatic interactions between the atomic cores. Thus, the total potential energy of a system containing n atoms, E_{tot}, can be written as

$$E_{\text{tot}} = \sum_{i}^{n} F_i(\varrho_i) + \frac{1}{2}\sum_{i}^{n}\sum_{j\neq i}^{n} \phi_{ij}(r_{ij}) \qquad (1)$$

where F_i is the embedding energy of atom i, i.e. the energy required to embed atom i into the electron density at location of atom i, ϱ_i, and $\phi_{ij}(r_{ij})$ is the pairwise interaction between atoms i and j separated by the distance, r_{ij}. The electron density at each site is computed from the superposition of spherically averaged atomic electron densities, i.e.

$$\varrho_i = \sum_{j\neq i}^{n} f_j^{\alpha}(r_{ij}) \qquad (2)$$

Here, $f_j^{\alpha}(r_{ij})$ is the atomic electron density at a distance r_{ij}, from the nucleus of atom j and the superscript α is used to specify the species of atom j.

In the present work, EAM-type interatomic potentials are used for both the γ-TiAl phase and the β-Ti–V phase. γ-TiAl has an $L1_0$ type ordered structure, and therefore when carrying out atomic simulations in this phase one must account for the Ti–Ti, Al–Al and Ti–Al interactions and for the fact that the two atomic species reside on separate sublattices. Farkas [21] recently developed the necessary EAM-type potentials for γ-TiAl and showed that reasonable agreement can be obtained between the model predictions and the experimentally measured properties of this phase. In the present work the Farkas potentials will be used to describe Ti–Ti, Al–Al and Ti–Al interactions within the γ-TiAl phase.

The β-Ti–V phase has a disordered (b.c.c.) structure, and to simplify the calculations the β-Ti–V phase is treated as a pseudomonoatomic phase composed of "effective" Ti–V atoms rather than individual Ti and V atoms. The derivation of the EAM potential functions for the pseudomonoatomic β-phase by applying an averaging scheme to the corresponding EAM functions of the constituent elements (Ti and V) was discussed in detail in a previous work [14]. The use of the pseudomonoatomic approximation for the Ti–V system can be justified because the two elements in question differ slightly in both atomic mass (47.90 for Ti and 50.94 for V) and electronegativity (1.4 for Ti and 1.9 for V) [22]. In our previous atomistic simulation work [14], it was shown that the use of effective Ti–V potentials leads to reasonable predictions of the number of properties of the β-phase. In particular, the b.c.c. structure was found to be unstable in pure Ti, metastable in Ti–15 at % V and stable in Ti–25 at % V relative to the h.c.p. structure at 0 and 100 K, which is consistent with the available thermodynamic data [23].

Atomistic simulations carried out in the present work were based on the use of a γ-TiAl–β-Ti–V computational bicrystal containing three types of atoms, i.e. the Ti and the Al atoms associated with the γ-TiAl phase and the effective Ti–V atoms constituting the Ti–V β-phase. Therefore, there are six distinct atomic pairs whose interactions (the ϕ_{ij} terms in Equation 1)

must be known. As mentioned earlier the pair potentials for the Ti–Ti, Al–Al and Ti–Al pairs along with the corresponding embedding energy functions for the γ-phase have been determined by Farkas [21]. The effective Ti–V atom/effective Ti–V atom pair potentials as well as the corresponding embedding energies have been derived in our previous work [14]. Hence there remains only two unknown interatomic parameters, the Ti/effective Ti–V atom and the Al/effective Ti–V atom pair potentials, which must be determined in order to be able to describe the atomic interactions completely in the γ–β computational bicrystal. The missing pair potentials, $\phi_{i\beta}$ (i = Ti, Al, β = the effective Ti–V atom), are constructed in the present work using Johnson's approach [24] as follows

$$\phi_{i\beta} = \frac{1}{2}\left[\frac{f_\beta(r_{\beta\beta})}{f_i(r_{ii})}\,\phi_{ii}(r_{ii}) + \frac{f_i(r_{ii})}{f_\beta(r_{\beta\beta})}\,\phi_{\beta\beta}(r_{\beta\beta})\right] \quad i = \text{Ti, Al} \tag{3}$$

where f_β and $\phi_{\beta\beta}$ are, respectively, the atomic electron density and the pair potential functions of the β-Ti–V phase, which are obtained using the aforementioned pseudomonoatomic approximation [14].

2.2. Computational crystal

2.2.1. Formation of the computational bicrystal

The γ-TiAl–β-Ti–V computational bicrystal was formed by bringing into contact two rectangular single crystals, one containing the γ-phase and the other consisting of the β-phase, Fig. 1. Prior to forming the bicrystal, the equilibrium lattice parameters at 100 K in each phase were determined. This was done using the EAM potential functions described in Section 2.1. and the quasiharmonic approximation method [14, 25]. For the $L1_0$ TiAl γ-phase the following lattice parameters were found: $a_\gamma = 0.3944$ nm and $c_\gamma = 0.4010$ nm, resulting in a c_γ/a_γ ratio of 1.05, which is in fair agreement with its experimental counterpart, $c_\gamma/a_\gamma = 1.03$ [26].

A β-phase with 15 at % V was chosen in the present work because it was found previously [14] that at this level of vanadium, the b.c.c. structure was metastable relative to the h.c.p. (martensite) phase with an activation energy barrier (0.001 eV per atom) for the b.c.c. → h.c.p. transformation. Consequently, only a limited extent of the b.c.c. → h.c.p. transformation was observed in the bulk b.c.c. Ti–15V crystal during the atomistic simulations at 100 K in the absence of stress. When a crack was introduced into the computational crystal, on the other hand, the associated stresses were found to give rise to a larger extent of martensitic transformation [17]. When the amount of vanadium was significantly less than 15 at % (say 10 at %), the b.c.c. phase was unstable and consequently the b.c.c. → h.c.p. transformation took place in the perfect stress-free crystal in the absence of stress. On the contrary, when the amount of vanadium was 20 at % or higher, the b.c.c. phase remained stable even in the presence of a mode I crack loaded to a stress level corresponding to the Griffith stress intensity factor [17]. For the Ti–15 V b.c.c. phase the EAM-base quasiharmonic calculation yielded the lattice parameter $a_\beta = 0.3186$ nm at 100 K, which was in reasonable agreement with its experimental counterpart (0.322 nm) [27].

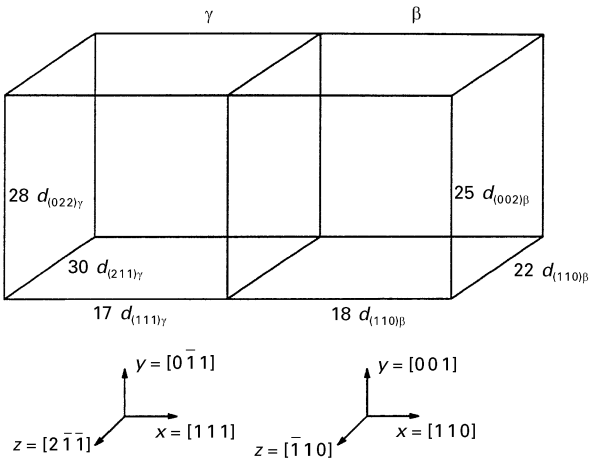

Figure 1 Computational γ-TiAl–β-Ti–15V bicrystal used in the present work.

In the γ-TiAl–β-Ti–V computational bicrystal used in the present work the following γ–β interface plane and the orientation relationship between the two phases were selected:

1. The interface plane was chosen to be parallel to the close-packed planes in the two structures, i.e. $(1\,1\,1)_\gamma \parallel (1\,1\,0)_\beta$, and the interface normal was aligned in the x-direction.
2. The $(0\,\bar{1}\,1)_\gamma$ plane was selected as the crack plane because this plane was frequently cited as the most likely cleavage plane in the $L1_0$ γ-TiAl structure [28]. The crack plane normal was aligned in the y-direction.
3. The most likely cleavage plane in the b.c.c. β structure, the $(0\,0\,1)_\beta$ plane [29], was next set parallel to the crack plane in the γ-phase.

The aforementioned procedure yielded the following orientation relationship between the two phases: $x \parallel [1\,1\,1]_\gamma \parallel [1\,1\,0]_\beta$, $y \parallel [0\,\bar{1}\,1]_\gamma \parallel [0\,0\,1]_\beta$ and $z \parallel [2\,\bar{1}\,\bar{1}]_\gamma \parallel [\bar{1}\,1\,0]_\beta$, Fig. 1. It should be noted that this orientation relationship is commonly referred to as the Nishiyama–Wasserman orientation relationship in the analysis of f.c.c.–b.c.c. interfaces in steels [30]. This orientation relationship was chosen in the present work because it enabled b.c.c. → h.c.p. $(\bar{1}\,1\,0)_\beta[1\,1\,0]_\beta$ transformation shuffling to take place in the x–y planes on the β side of the computational crystal without being interfered with by the periodic boundary conditions applied in the z-direction.

The size of the computational bicrystal used in the present work, in terms of the number of interplanar spacings, $d_{(uvw)}$ of the $(u\,v\,w)$ planes, was as follows: $17d_{(1\,1\,1)} \times 28d_{(0\,2\,2)} \times 30d_{(2\,1\,1)}$ for the γ-phase and $18d_{(1\,1\,0)} \times 25d_{(0\,0\,2)} \times 22d_{(1\,1\,0)}$ for the β-phase, respectively. The bicrystal contained 10 654 atoms (2610 Ti, 2610 Al and 5434 equivalent Ti–V atoms). With this size of computational bicrystal, the two crystals had the following dimensional mismatches in the plane of the interface: 0.49% mismatch in the $y \parallel [0\,\bar{1}\,1]_\gamma \parallel [0\,0\,1]_\beta$ direction and a 0.70% mismatch

in the $z \parallel [2\,\bar{1}\,\bar{1}]_\gamma \parallel [\bar{1}\,1\,0]_\beta$ direction. No attempt was made to remove these dimensional mismatches by stretching and/or compressing the two crystals.

In addition to specifying the γ–β orientation relationship, the relative stacking of the atoms in the two structures must be defined. The $(1\,1\,1)_\gamma$ and $(1\,1\,0)_\beta$ planes, which are parallel to the γ–β interface have, respectively, *ABCABC*- and *ABAB*-types of atomic stacking. The two crystals were stacked in such a way that in the middle of the computational crystal the $(1\,1\,0)_\beta$ plane nearest to the interface "coincides" with the $(1\,1\,1)_\gamma$ plane, which was the next nearest to the interface and vice versa, and yielded the stacking sequence $A_\gamma B_\gamma C_\gamma A_\gamma B_\gamma | A_\beta B_\beta A_\beta B_\beta \ldots$.

Before creating a crack in the γ-crystal, the structure of the computational bicrystal was minimized using molecular statics under periodic boundary conditions in the *y*- and *z*-directions and free surface boundary conditions in the *x*-direction. The use of free surface boundary conditions in the *x*-direction allowed the interplanar spacings of the planes parallel to and near the γ–β interface to adjust to the presence of different atomistic species in the associated planes in the other phase. The structure of the γ–β interface after the aforementioned energy minimization procedure is shown in Fig. 2. It is seen that the mismatch in the number of associated planes in the two phases across the γ–β interface has been accommodated by the formation of appropriate interfacial dislocations: the first type of interfacial dislocations, type A, have the line direction, $l = [2\,\bar{1}\,\bar{1}]_\gamma \parallel [\bar{1}\,1\,0]_\beta$ and the Burger's vector, $b = 1/2[0, \bar{a}_\gamma, c_\gamma]_\gamma \parallel a_\beta[0\,0\,1]_\beta$, Fig. 2a. There are three A-type dislocations in Fig. 2a with interdislocation spacings of $\sim 9 d_{(0\,2\,2)_\gamma}$ or $8 d_{(0\,0\,2)_\beta}$. The other interfacial dislocations, type B, have the line direction, $l = [0\,\bar{1}\,1]_\gamma \parallel [0\,0\,1]_\beta$ and the Burger's vector, $b = a_\gamma[1\,0\,0]_\gamma \parallel a_\beta[0\,1\,0]_\beta$, Fig. 2b. There is only one of these dislocations per periodic length in the *z*-direction, i.e. the interdislocation spacing is $\sim 28 d_{(2\,2\,0)_\gamma}$ or $25 d_{(0\,0\,2)_\beta}$. As shown in Fig. 2c the A and B interfacial dislocations run, respectively, parallel to the *z*- and *y*-edges of the computational bicrystal and hence intersect at a right angle.

It should be pointed out that because of the use of periodic boundary conditions during the energy minimization procedure, the γ–β interface was constrained to remaining parallel to the *y*–*z* plane. However, it is well established in the literature dealing with austenite–ferrite interfaces in steels [30], that the matching of the two phases can be significantly improved and hence the energy reduced if structural ledges are allowed to form on the $(1\,1\,1)_{\text{austenite}} \parallel (1\,1\,0)_{\text{ferrite}}$ interface. Such ledges, which are in fact interfacial dislocations, divide the interface into regions of good atomic matching with the orientation $(1\,1\,1)_{\text{austenite}} \parallel$

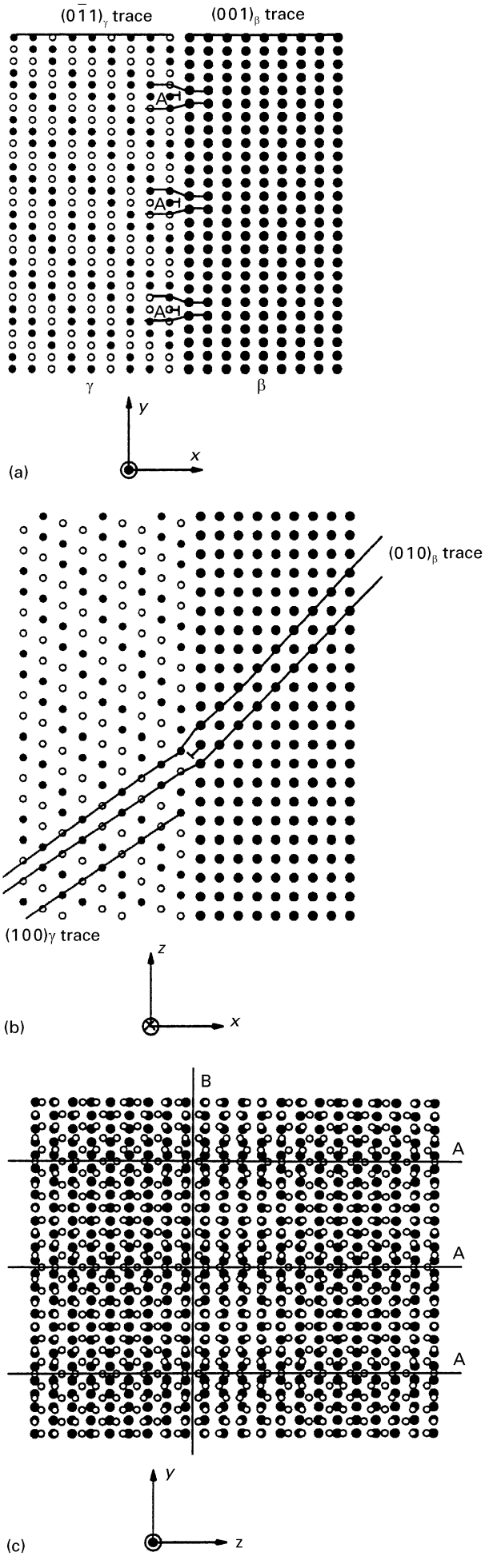

Figure 2 Equilibrium structure of the γ-TiAl–β-Ti–15V interface: (a) atomic positions projected onto the $(2\,\bar{1}\,\bar{1})_\gamma \parallel (\bar{1}\,1\,0)_\beta$ planes, (b) atomic positions projected onto the $(0\,\bar{1}\,\bar{1})_\gamma \parallel (\bar{0}\,0\,1)_\beta$ planes and (c) interface structure by projections of two $(1\,1\,0)_\gamma$ and two $(1\,1\,1)_\beta$ planes beside the interface. For (a) and (c): (○) Ti, (●) Al, (●) β-Ti–15V. For (b): (○) γ(Ti, Al), (●) β-Ti–15V.

$(1\,1\,0)_{\text{ferrite}}$ and in such cases the macroscopic interface generally corresponds to a high index plane. It is very likely that the structural ledges would form in the case of γ-TiAl–β-Ti–V interfaces, and hence the interaction of a crack with such interfaces should be considered. This was not done in the present work, however, because due to the resulting deviation of the interface from the $(1\,1\,1)_\gamma \parallel (1\,1\,0)_\beta$ orientation, the crack would no longer be normal to the interface and one of the assumptions made in the present analysis could not be satisfied.

2.2.2. Generation of a crack in the initial computational bicrystal

To carry out the atomistic simulations of martensitic transformation and the resulting toughness enhancement in the dispersed β-phase when the transformation is induced by the stress concentration accompanying the formation of cracks in the γ-matrix, the case of a crack located in the γ-phase whose tip touches the γ–β interface subject to a uniaxial mode I external loading is studied in the present work, Fig. 3. The singular stresses and the corresponding displacements that dominate the near crack-tip stress and displacement fields have been derived and analysed in Part I of this paper [18]. These fields are utilized in the present work to generate a crack in the computational bicrystal and to apply the appropriate boundary conditions to it. As shown in Part I, the external mode I loading gives rise in the case of a crack touching the γ–β interface to a singular stress field composed of two terms (named A and B for convenience) with distinct orders of stress singularity

$$\sigma_{ij}(r,\theta) = \frac{K_A}{r^{1-\lambda_A}} h_{A_{ij}}(\theta) + \frac{K_B}{r^{1-\lambda_B}} h_{B_{ij}}(\theta) \quad i,j = r,\theta \qquad (4)$$

where K_A and K_B represent the generalized stress intensity factors, λ_A and λ_B the corresponding orders of the stress singularity, $h_{A_{ij}}(\theta)$ and $h_{B_{ij}}(\theta)$ the corresponding angular dependences of the stresses, and θ is the polar angle.

The corresponding (plane strain) displacement field also contains two terms, each with a distinct order of stress singularity

$$u_i(r,\theta) = K_A r^{\lambda_A} f_{A_i}(\theta) + K_B r^{\lambda_B} f_{B_i}(\theta) \quad i = r,\theta$$

$$u_z(r,\theta) = 0 \qquad (5)$$

where $f_i(\theta)$ is the angular displacement function.

The two orders of stress singularity for the γ–β computational bicrystal were found in Part I to be $\lambda_A = 0.4789$ and $\lambda_B = 0.4114$. Also, the angular functions for the stress, $h_{ij}(\theta)$, and for the displacement, $f_i(\theta)$, were determined and by analysing the symmetry of these functions relative to θ, it was concluded that the two terms in the singular stress and displacement fields, Equations 4 and 5, do not correspond to either the pure mode I nor the pure mode II fields. Mode A was found to be more mode I-like, while mode B was more mode II-like. The magnitudes of the two generalized stress intensity factors, K_A and K_B, corresponding to a reference level of the externally applied stress were also determined. Since K_A and K_B both scale with the magnitude of the externally applied stress their magnitudes at any other level of applied stress can be obtained using the appropriate scaling constant.

The (atomistic) computational bicrystal used in the present work is, as is generally the case, too small to reliably represent the entire physical system of interest, i.e. a crack in the γ-matrix impinging on the interface of a γ-phase and dispersed γ-phase particle. To overcome this problem the computational bicrystal is embedded into the continuum bicrystal, Fig. 3b.

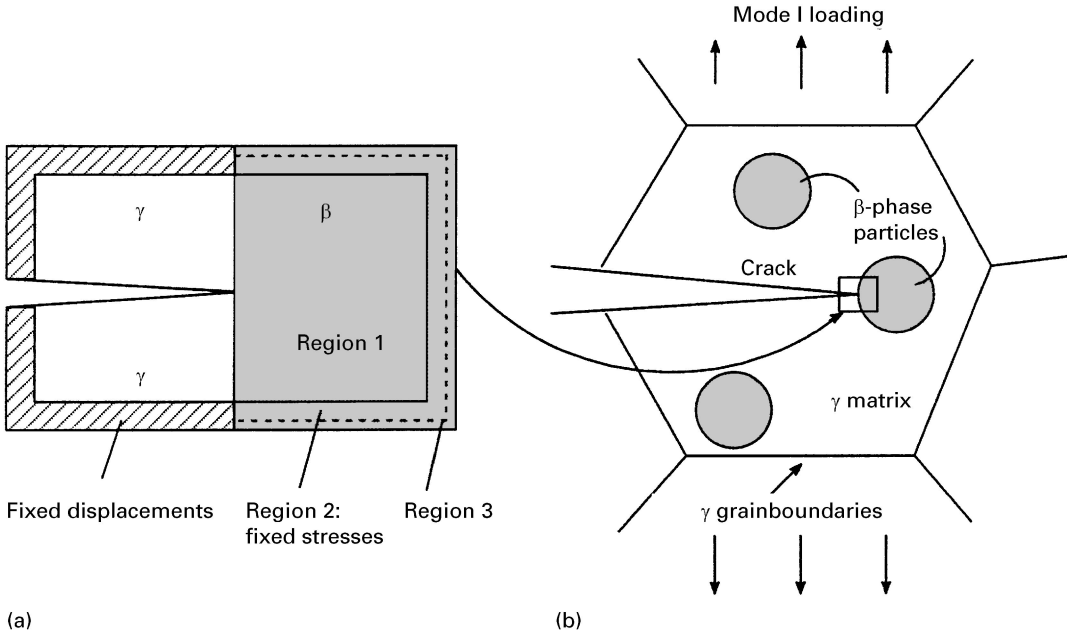

Figure 3 (a) Computational bicrystal with a crack in the γ-phase touching the γ–β interface and (b) the relationship between the computational bicrystal and the typical γ–β two-phase microstructure observed in [3].

The effect of the (exterior) continuum bicrystal on the interior atomistic bicrystal is taken into account by imposing the appropriate boundary conditions on the border atoms of the atomistic bicrystal. In the present case, the following boundary conditions were used:

1. To achieve the plane strain condition, fixed periodic boundary conditions were used in the z-direction, the crack-front direction:

2. To prevent γ–β interfacial dislocations from escaping to the free surface by gliding along the interface, fixed displacement boundary conditions were applied on the three atomic layers of the γ-phase in x- and y-directions. The magnitudes of the (fixed) displacements at a given level of (generalized) stress intensity factors have been determined using Equation 5:

3. Fixed displacement boundary conditions cannot be used in the case of the β-phase because such conditions were found in our previous work [17] to interfere with the b.c.c. → h.c.p. martensitic transformation in this phase by preventing the $(1\,1\,0)_\beta[\bar{1}\,1\,0]_\beta$ transformation shuffling from taking place. Instead, fixed stress boundary conditions were used for the β-phase in the x- and y-directions. The fixed stress boundary conditions prescribed on the three outermost atomic layers of the β-phase were obtained using Equation 4.

Consequently, as shown in Fig. 3a, three distinct atomic regions can be identified in the β-phase. In region I, no external stresses (forces) are applied to the atoms that are allowed to move freely in response to the atomic interaction forces during the molecular dynamics simulation runs. In region II, the atoms are subject to fixed stress boundary conditions but are otherwise free to move. The role of region III is to provide atoms that act as neighbours to the atoms in the region II, and thus ensure a bulk-like environment as opposed to free surface co-ordination for the atoms in region II.

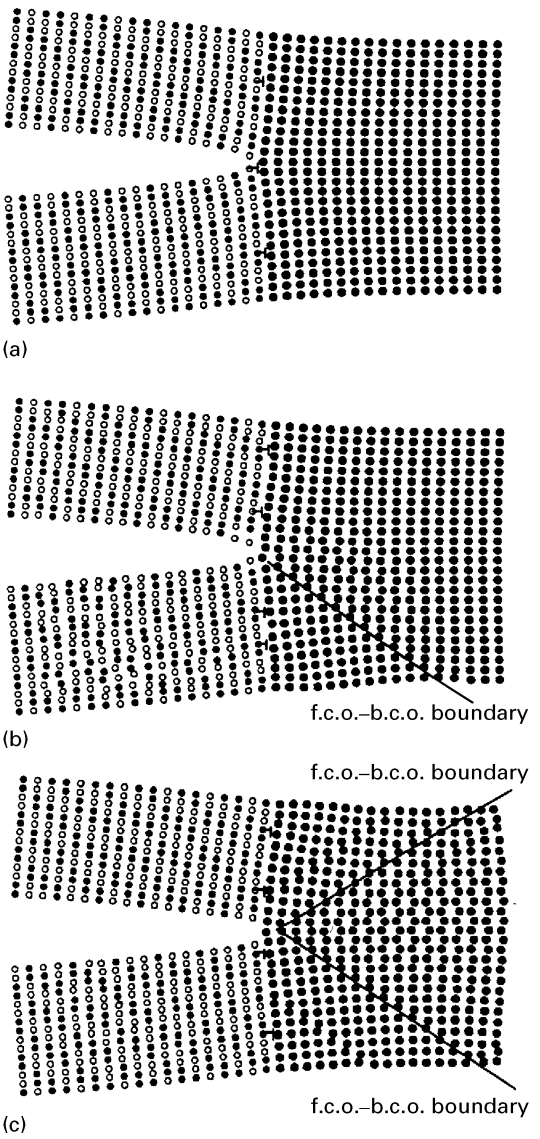

Figure 4 Evolution of atomic positions in the γ-TiAl–β-Ti–15V bicrystal with a crack projected on the $(2\,\bar{1}\,\bar{1})_\gamma \parallel (\bar{1}\,1\,0)_\beta$ planes as a function of simulation time: (a) 0 ps, (b) 1 ps, (c) 10 ps. (○) Ti; (●) Al; (●) β-Ti–15V; (+) interfacial dislocations, $b = 1/2[0\,\bar{a}_\gamma\,c_\gamma]$.

2.3. Computational method

The evolution of the material in the region around the crack tip is studied by carrying out standard molecular dynamics calculations in the computational bicrystal described above. Within the molecular dynamics scheme, the classical equations of motion for the atoms are solved to determine the atomic positions and velocities in the computational bicrystal as a function of time [31]. The method is therefore suitable for studying time-related phenomena, such as phase transformations crack and dislocation propagations, etc. All the molecular dynamics calculations presented in this work were carried out at 100 K. To obtain this temperature, each atom was initially assigned a random velocity from the corresponding Boltzmann distribution. To maintain the simulation temperature at 100 K, exponential relaxation of the average squared velocity with a time constant of 0.1 ps was applied at each time step (2 fs). This allowed the temperature to be maintained within $\pm 2\%$ of the desired temperature.

3. Results and discussion

As described in Section 2.2.2, the initial crack in the γ-phase portion of the γ–β computational bicrystal has been created by displacing the atoms in accordance with Equation 5. The finite element procedure for computing the magnitude of the two generalized stress intensity factors, K_A and K_B, corresponding to a given level of the average uniaxial stress in the y-direction (applied under the constant remote displacement conditions in the same direction) has been discussed in Part I [18]. The initial atomic configuration in the bicrystal with a crack in the γ-phase, subject to an average remote stress level of 180 MPa is shown in Fig. 4a. It should be noted that due to the introduction of a crack into the computational bicrystal one of the $b = 1/2\,[0\,\bar{a}_\gamma\,c_\gamma]_\gamma \parallel a_\beta[0\,0\,1]_\beta$ interfacial dislocations is located at the crack tip with its extra-half-plane becoming one of crack surfaces. The other interfacial dislocations were not significantly affected by the introduction of the crack.

The progress of the material's evolution at the crack tip as a function of simulation time is shown in Fig. 4. After about 1 ps of simulation time, Fig. 4b, the two crack faces in the near vicinity of the crack tip are seen to have moved outwards a little bit. This movement is clearly related to the observed sliding of the $b = 1/2[0\,\bar{a}_\gamma\, c_\gamma]_\gamma \| a_\beta[0\,0\,1]_\beta$ interfacial dislocations along the γ–β interface and away from the crack tip as well as with the relaxation of the atoms at the crack surface. As a result of these crack-tip processes, an additional extra $(0\,\bar{1}\,1)_\gamma$ plane has been created making a total of four $b = 1/2[0\,\bar{a}_\gamma\, c_\gamma]_\gamma$ interfacial dislocations.

The atomic configuration shown in Fig. 4c suggests, as was expected, that with the exception of some minor atomic rearrangement, there are no phase transformations in the γ-phase. In sharp contrast, the β-phase region ahead of the crack tip has to undergo significant changes in its structure at this stage. The region in the β-phase corresponding to $\sim -40^\circ \leqslant \theta \leqslant 40^\circ$ (θ is the polar angle), has transformed into a b.c.c. structure with a two atom basis. In the regions of the β-phase corresponding to $-90^\circ \leqslant \theta \leqslant -40^\circ$ and $40^\circ \leqslant \theta \leqslant 90^\circ$, on the other hand, an f.c.o. structure is observed.

These findings are consistent with common experimental observations [32], which show that, while several different martensites structures exist in the transformed β-phase, only two, a h.c.p. α′ structure and f.c.o. α″ structure exist in the bulk material. The others, generally observed under a transmission electron microscope, appear to be the result of a thin-film effect [32]. The α′ martensite is most prevalent in pure or low-alloyed Ti. The A″ martensite, on the other hand, is commonly observed in Ti-base alloys containing a higher level of β stabilizing elements (such as V, Nb, Ta, etc.) and as a result of stress–strain-induced martensitic transformation [32].

According to Burgers [33], the b.c.c. → h.c.p. martensitic phase transformation can be described in terms of the following two elemental processes: (a) shuffling of the parallel adjacent $(1\,1\,0)_{\text{b.c.c.}}$ planes in the opposite $[1\,\bar{1}\,0]_{\text{b.c.c.}}$ directions by an amount of $1/6d_{(1\,1\,0)\,\text{b.c.c.}}$, where d refers to the corresponding interplanar spacing; and (b) a pure shear on the $\{1\,1\,2\}_{\text{b.c.c.}}$ planes in the $\langle 1\,1\,\bar{1}\rangle_{\text{b.c.c.}}$ directions. The shuffling displacements produce the characteristic h.c.p.-type *ABAB* stacking of the close packed $(0\,0\,0\,1)_{\text{h.c.p.}}$ planes. The transformation shear, on the other hand, converts an irregular hexagonal atomic arrangement in the $(1\,1\,0)_{\text{b.c.c.}}$ planes with the characteristic angle $\theta = 109.47^\circ$ into a regular hexagonal atomic arrangement ($\theta = 120^\circ$) in a close-packed $(0\,0\,0\,1)_{\text{h.c.p.}}$ plane. The b.c.o. structure observed in the present work, Fig. 4b and c, has been produced by the operation of the same two elemental processes, i.e. by $\{1\,1\,0\}_\beta\langle\{1\,\bar{1}\,0\rangle_\beta$ shuffling and by $\{1\,1\,2\}_\beta\langle 1\,1\,\bar{1}\rangle_\beta$ shear, but the magnitudes of the shuffling displacements and transformation shear are smaller than their counterparts in the case of the b.c.c. → h.c.p. transformation. In fact, the h.c.p. structure can be considered as a b.c.o. structure in which additional relations exist between the lattice parameters: $a_{\text{h.c.p.}} = (3)^{1/2} b_{\text{h.c.p.}} = (3/8)^{1/2} c_{\text{h.c.p.}}$

The results shown in Fig. 4b and c, suggest that formation of the f.c.o. martensites is closely related to the presence of a γ–β interface and, in particular, is affected by high stresses on the β-phase side of the interface that have tensile characters because the extra-half-planes of the $b = 1/2[0\,\bar{a}_\gamma\, c_\gamma]_\gamma$ dislocations reside in the γ-phase.

In order to conduct a more detailed analysis of the martensitic transformation in the β-phase portion of the computational bicrystal, three atomic configurations, corresponding to the one in Fig. 4c, but each at a different value of the z-co-ordinate are shown in Fig. 5. In each case only the projections of the atoms in the alloy residing on three adjacent parallel $(\bar{1}\,1\,0)_\beta$ planes are shown. A number of important findings can be made based on the results shown in Fig. 5.

1. Transformation shuffling is seen to take place in the $[1\,1\,0]_\beta$ direction at some values of the z-co-ordinate in the β crystal and in the $[\bar{1}\,\bar{1}\,0]_\beta$ direction at the others relative to the layer's original position (compare configurations X and Y at $z = 0$–$2d_{(1\,1\,0)_\beta}$ and $z = 10$–$12d_{(1\,1\,0)\beta}$. In addition, the direction of transformation shear varies with the z co-ordinates. This finding appears to be related to the use of fixed periodic boundary conditions in the z-direction, and is the manifestation of the self-accommodation of the shape change accompanying the transformation:

2. The f.c.o. martensite phase undergoes a slip deformation due to the passage of the edge dislocations with the line direction, $l = \langle 1\,1\,\bar{2}\rangle_{\text{f.c.o.}}$, the Burger's vector, $b = a_{\text{f.c.o.}}/2\langle\bar{1}\,1\,0\rangle_{\text{f.c.o.}}$ and the $\{1\,1\,1\}_{\text{f.c.o.}}$ slip plane, Fig. 5c. Different $\{1\,1\,1\}_{\text{f.c.o.}}$ planes act as slip planes along the z-direction of the crystal, which is again an indication of the self-accommodation of the b.c.c. → f.c.o. transformation shape change. Because the $b = a_{\text{f.c.o.}}/2\langle\bar{1}\,1\,0\rangle_{\text{f.c.o.}}$ dislocations are the unit dislocations in the f.c.o. structure, their motion causes the shape but not the structural change in the f.c.o. phase. The emission of these dislocations from the γ–β interface near the crack tip acts as a lattice invariant deformation mechanism that is an integral part of the b.c.c. → f.c.o. martensitic transformation:

3. The orientation relationships between the parent β-structure and the two martensitic structures were determined as

$$(\bar{1}\,1\,0)_{\text{b.c.c.}} \| (0\,0\,1)_{\text{f.c.o.}} \| (0\,0\,1)_{\text{b.c.o.}}$$

$$[1\,1\,1]_{\text{b.c.c.}} \| [\bar{1}\,1\,0]_{\text{f.c.o.}} \| [\bar{1}\,1\,0]_{\text{b.c.o.}}$$

which is in excellent agreement with the selected area electron diffraction (SAD) analyses in Ti–10V–3Al–2Fe β-alloy [34].

In order to clarify further the effect of the β-phase on the evolution of the materials at crack tip and on the crack behaviour, the molecular dynamics analysis has been extended to include the cases of a single-phase γ crystal and a single-phase β crystal each containing a crack. The orientation of the computational crystal as well as of the crack in these single-phase material simulations were selected in such a way that they match their corresponding counterparts given in Fig. 1. The generation of a crack in the single-phase material is quite straightforward and is

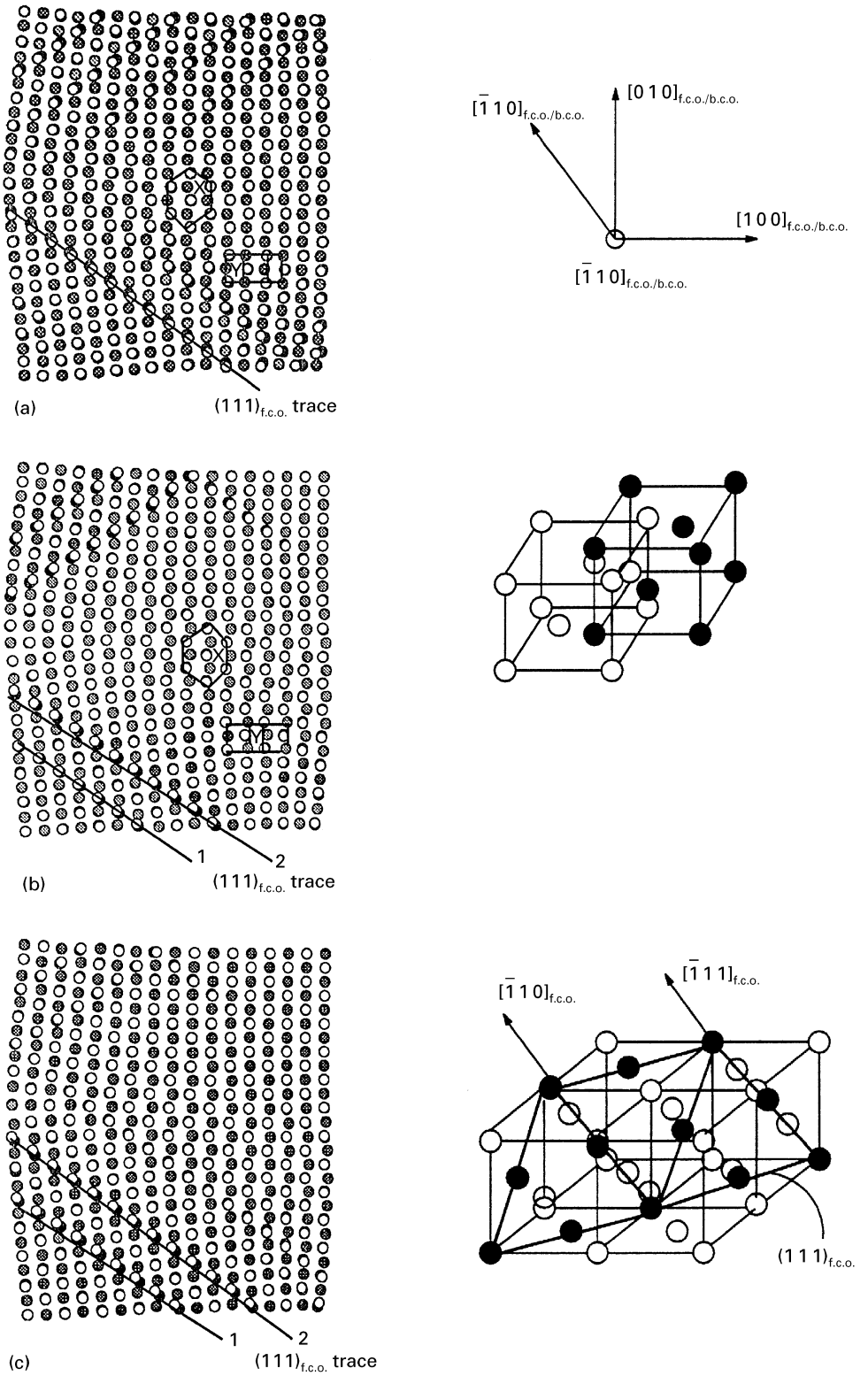

Figure 5 Atomic positions in the β-phase projected on the $(\bar{1}\,1\,0)_\beta$ planes at 10 ps of molecular dynamics simulation time: (a) $z = 0$–$2d_{(1\,1\,0)_\beta}$, (b) $z = 10$–$12d_{(1\,1\,0)_\beta}$ and (c) $z = 12$–$14d_{(1\,1\,0)_\beta}$. Schematic representations of the transformed b.c.o. and f.c.o. structures along with their slip systems were also given in (b) and (c).

done by displacing the atoms from their perfect-crystal positions using the plane-strain linear (anisotropic) elastic solution for the mode I displacement functions as developed by Sih and Liebowitz [35]

$$u_i(r,\theta) = K_I(2r/\pi)^{1/2} f_i(\theta) \quad (i = r,\theta)$$

$$u_z(r,\theta) = 0 \tag{6}$$

where r and θ are the polar co-ordinates. The coefficients in the angular displacement function, $f_i(\theta)$, depend on the crystal orientation and the crack orientation through the orientation dependence of the elastic constants of the materials [13]. K_I is the usual mode I stress intensity factor. Equation 6 is a special case of Equation 5, in which, due to the fact that the crack resides in a single material, the two singular terms in

Equation 5, which are of pure mode I and pure mode II character, are completely decoupled and hence a pure mode I loading activates only the pure mode I displacement (and stress) field. In addition, the order of stress singularity, $\lambda = 0.5$, is equal for both singular terms in Equation 5. It should also be recalled that the mode I stress intensity factor has a critical value corresponding to the reversible self-similar extension of the crack, the Griffith stress intensity factor, K_{Gr}

$$K_{Gr} = (2\gamma/A)^{1/2} \quad (7)$$

where γ is the surface energy of the crack plane and A is a parameter that is defined in terms of the elastic constants of the crystal. For the crack–crystal orientation specified in Fig. 1, Equation 7 yielded the following values for the Griffith stress intensity factor: $K_{Gr} = 0.76\ \text{MPa min}^{1/2}$ in single-phase γ and $K_{Gr} = 0.54\ \text{MPa m}^{1/2}$ in single-phase β. A more detailed account of the calculation of the Griffith stress intensity factor is given elsewhere [13].

Because the generalized stress intensity factors, K_A and K_B, in Equations 4 and 5 and the mode I stress intensity factor, K_I, in Equation 6 have different units, it is not possible to compare the crack behaviour in the single-phase and the two-phase materials at the same level of stress intensity factor. Instead, the crack behaviour was compared at the same level of the remotely applied average stress (180 MPa). As explained in Part I of this paper [18], the stress is applied using the constant displacement boundary conditions at the edges of the finite element computational crystal. Under these conditions, the enriched-finite element formulation presented in Part I [18], yielded the following values of the mode I stress intensity factors in the two single-phase materials: $K_I = 1.06\ \text{MPa m}^{1/2} = 1.39K_{Gr}$ in single γ and $K_I = 0.81\ \text{MPa m}^{1/2} = 1.50K_{Gr}$ in single β. These values of stress intensity factors were next used in conjunction with Equation 6 to displace the atoms in order to create a crack in the two single-phase materials.

The molecular dynamics simulation results for the single-phase γ crystal containing a crack subject to the same type of boundary conditions as the one applied to the γ part of the computational bicrystal in Fig. 3, i.e. the fixed displacement boundary conditions in the x- and y-directions and the fixed periodic boundary conditions in the z-direction, are shown in Fig. 6. The crack is seen to propagate initially along the original $(0\,\bar{1}\,1)_\gamma$ crack plane. However, at a later stage of crack propagation, the crack temporarily leaves its original crack plane and begins to advance along the $(\bar{2}\,\bar{5}\,1)_\gamma$ plane before it turns back onto another $(0\,\bar{1}\,1)_\gamma$ plane, Fig. 6b. The crack propagation appears to involve only bond breaking with no visible dislocation emission and hence the fracture mode in single-phase γ can be characterized as brittle cleavage.

Fig. 7 shows the results of our molecular dynamics simulation of crack propagation in single-phase β under boundary conditions identical to those applied to the β part of the γ–β bicrystal in fixed stress boundary conditions in the x- and y-directions and periodic boundary conditions in the z-direction. For clarity

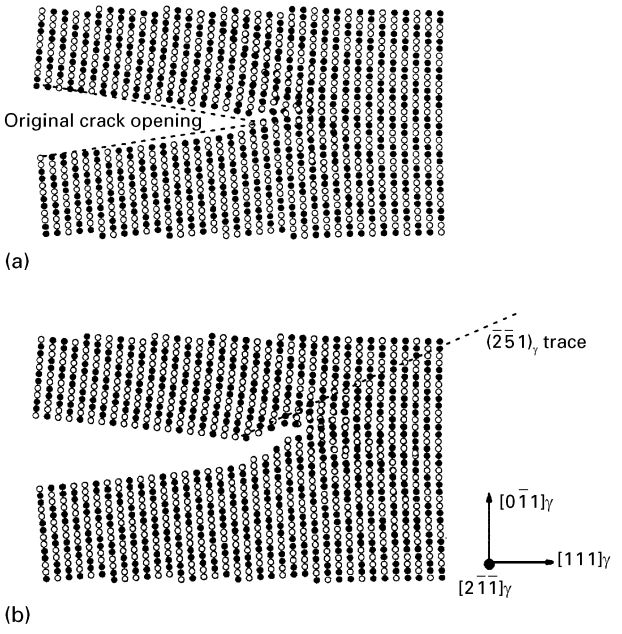

Figure 6 Atomic positions in the single-phase γ-TiAl crystal with a crack projected on the $(2\,\bar{1}\,\bar{1})_\gamma$ plane after (a) 1 ps and (b) 10 ps of the simulation time: (○) Ti, (●) Al.

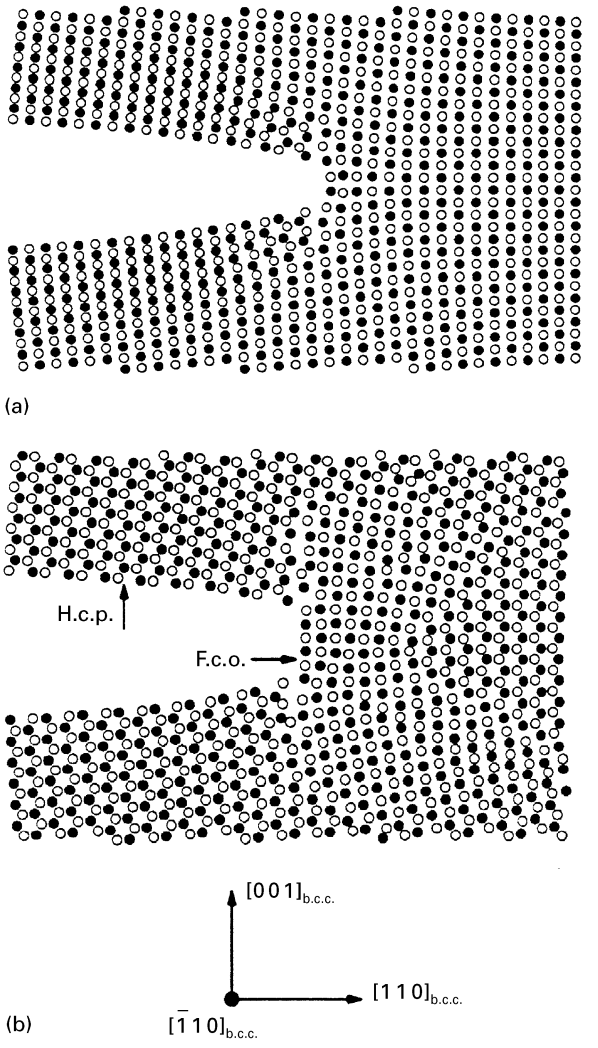

Figure 7 Atomic positions in the single-phase β-Ti–15V crystal with a crack projected on the $(1\,1\,0)_\beta$ plane at (a) 0.4 ps and (b) 3 ps of the simulation time: (○) Ti, (●) Al.

only the innermost atoms near the crack-tip region are shown and the open and filled circles are used to differentiate between the atoms residing on two adjacent $(1\,1\,0)_{\text{b.c.c.}}$ planes.

The first evidence for the formation of an h.c.p. phase was seen at about 0.4 ps and only on a portion of the crack surface close to the crack tip. As described earlier, the b.c.c. → h.c.p. martensitic transformation involves $\{1\,1\,0\}_{\text{b.c.c.}}\langle\bar{1}\,1\,0\rangle_{\text{b.c.c.}}$ shuffling and $\{1\,1\,2\}_{\text{b.c.c.}}\langle 1\,1\,\bar{1}\rangle$ pure shear. Ultimately the transformation front moves into the region ahead of the crack tip, but as seen in Fig. 7b, the very crack-tip region resists the b.c.c. → h.c.p. transformation and instead acquires an f.c.o. structure. The resistance of the crack-tip region towards the b.c.c. → h.c.p. transformation is consistent with the fact that there is a relatively large negative volume change ($\sim -5\%$) associated with this transformation [17] and hence the region ahead of the crack tip which is under the largest positive hydrostatic stress opposes the transformation the most. Consequently a f.c.o., which is associated with a smaller negative transformation volume change ($\sim -3\%$), rather than a h.c.p. structure forms at the crack tip. As a result of the observed transformation processes, the crack tip became blunt and despite the fact that the applied stress intensity factor exceeded the Griffith stress intensity factor by 50%, the crack did not advance any further.

To quantify the effect of martensitic transformation on the toughness of materials in single-phase crystals, the Eshelby's conservation integral, F [36], which provides a means for determination of the energy release rate accompanying crack extension in cases where plasticity effects cannot be neglected, was evaluated. The component of Eshelby's integral along the crack propagation direction x, F_1, which represents the force acting to propagate the crack tip, is given by

$$F_1 = \int_\Gamma \left[W\,\delta_{1j} - \sigma_{kj}\frac{\partial u_k}{\partial x_1}\right] \mathrm{d}S_j \qquad (8)$$

where W is the crystal strain energy density; u_k is the k-component ($k = x, y$) of the displacement; σ_{kj} are the stress components; $\mathrm{d}S_j = \mathrm{d}S \times n_j$, here n_j is the j component ($j = x, y$) of the unit outward normal vector to the contour segment of length $\mathrm{d}S$; and Γ a closed contour surrounding the crack. In the present work Γ was chosen as a circle centred at the crack tip with the radius of 4 nm. The magnitude of F_1 in the initial atomic configuration in the β-phase, the configuration obtained by displacing the atoms according to the mode I linear elastic solution, Equation 6, is given within the linear elastic continuum approximation as AK_I–2γ [13]. The computation of F_1 for an atomistic crystal based on Equation 8 requires the knowledge of the strain energy density, and the stress and strain components. These can be computed from the available EAM interatomic potential functions using the procedures, described elsewhere [7, 13]. To ensure the validity of Equation 8, the contour radius (4 nm) was chosen in such a way that it was at least three times as large as the radius of the transformation zone.

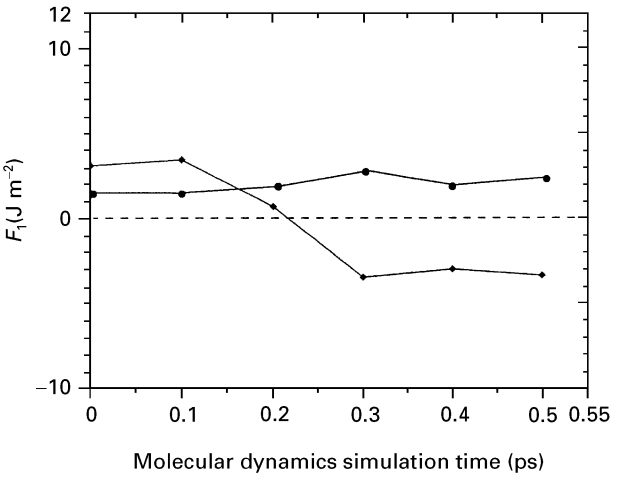

Figure 8 Time dependence of the F_1 integral in the single-phase γ (●) and single-phase β (◆) crystals.

The results depicted in Fig. 8 show the variation of the F_1 integral computed in both single-phase γ and single-phase β crystals as a function of molecular dynamics simulation time. In the γ-phase, the F_1 integral, i.e. in the force trying to extend the crack, increases slightly with simulation time, which is consistent with the observed propagation of the crack by brittle cleavage. In sharp contrast, the crack-tip martensitic transformation in the β-phase gives rise to a substantial reduction in the force, F_1, trying to extend the crack. In fact, after 0.25 ps this force becomes negative, implying that no further propagation of the crack should take place. This finding provides a quantitative explanation for the transformation-induced crack arrest observed in Fig. 7.

By comparing the atomic configurations shown in Fig. 4 (γ–β bicrystal). Figs 6 and 7 for the γ and β crystals, respectively, each corresponding to the same level of remotely applied stress, a number of important findings can be made regarding the effect of martensitic transformation in the β-phase on crack behaviour in the γ-phase:

1. While the crack readily extends in the single-phase γ crystal, Fig. 6, its propagation ceases when a β-phase is present in the region ahead of the crack tip, Fig. 4. This represents clear evidence for β-phase induced toughening.

2. The observed toughening effect must be related to the accompanying martensitic transformation (lattice-invariant slip deformation included) because almost the entire β crystal has undergone such transformation, Fig. 4.

3. The presence of the γ–β interface has a significant effect on the evolution of the materials at the crack tip. Specifically, the crack-tip opening displacement remains smaller in the γ–β case, Fig. 4, compared with that in the case of the single-phase β crystal, Fig. 7.

At last, it is interesting to compare the effectiveness of martensitic transformation in enhancing the fracture toughness in the two-phase γ–β bicrystal with that in the single-phase β crystal. Ideally, one would

like to be able to evaluate the magnitude of the F_1 integral in the γ–β bicrystal and compare it with the corresponding value in the β crystal. However, it must be noted that Equation 8, which is used to evaluate the F_1 integral in the single-phase materials, can only be applied if the field quantities (stress, strain, displacement) are continuous along the integration contour, Γ. Because this condition of continuity of the field quantities is not satisfied (e.g. σ_{rr} is discontinuous across the γ–β interface [18]), Equation 8 cannot be used in the case of the γ–β bicrystal. To overcome this problem, we recall the original definition of the energy release rate (the J integral) in non-linear elastic materials

$$J = -\frac{1}{L}\frac{\mathrm{d}\Pi}{\mathrm{d}a} \tag{9}$$

where Π and L are, respectively, the potential energy and the thickness of the crystal, and a is the crack length. The potential energy is given by

$$\Pi = U - W \tag{10}$$

where U is the strain energy of the body and W the work done by the external force. If the crack extends under the condition of fixed boundary displacement, (Δ = constant), there is no change in the work done by the external force, $\mathrm{d}W = 0$. Hence, combination of Equations 9 and 10 leads to

$$J = -\frac{1}{L}\left(\frac{\mathrm{d}U}{\mathrm{d}a}\right)_{\Delta} \tag{11}$$

Because the strain energy, U, for the γ–β computational crystal can be readily evaluated by summing up the strain energy of all the atoms in the bicrystal, Equation 11 is used in the present work to quantify the extent of toughening due to transformation. This was done using the following procedure:

1. Under the assumption that Equations 4 and 5 can be used when the crack tip is only a few atomic spacings away from the interface plane, a series of atomic configurations are generated, each corresponding to the same level of applied stress (180MPa) but with the crack tip shifted by $1–4d_{(1\,1\,0)_\gamma}$ into the γ-phase or $1–4d_{(1\,1\,0)_\beta}$ into the β-phase.

2. Each configuration is next relaxed through the use of molecular dynamics simulations, for the same simulation time (e.g. 1 ps) under the boundary conditions described in connection with Fig. 3.

3. The positions of the boundary atoms are set to coincide with those in the case of the crack tip residing on the γ–β interface and the molecular dynamics simulation runs repeated. The last step prior to running the simulations ensures that all the atomic configurations analysed correspond to the same boundary displacements as required by Equation 11.

4. The $(\mathrm{d}U/\mathrm{d}a)_\Delta$ term in Equation 11 is next evaluated using a finite difference approximation, i.e.

$$\left(\frac{\mathrm{d}U}{\mathrm{d}a}\right)_{\Delta} = \frac{E^R_{a+\Delta a} - E^R_a}{\Delta a} = \frac{1}{\Delta a}\sum_{i=1}^{n_R}\left(E^i_{a+\Delta a} - E^i_a\right) \tag{12}$$

where E^R_a and $E^R_{a+\Delta a}$ refer to the energy of a circular cylinder with a radius, R, and a centre at the γ–β interface, where the crack tip is located at a and $a + \Delta a$, respectively. E^i pertains to the energy of atom i in such a cylinder and n_R is the total number of atoms in the cylinder.

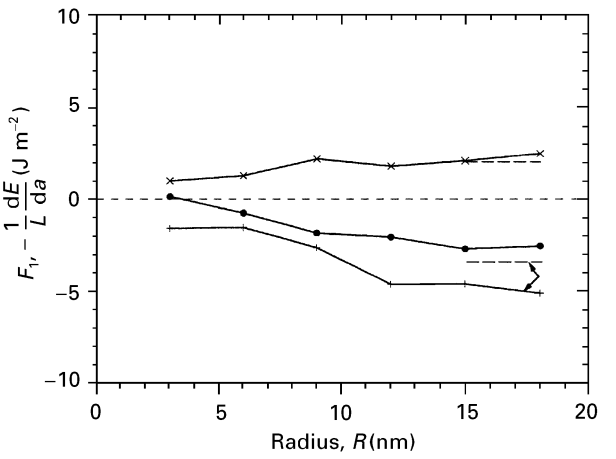

Figure 9 The dependence of circular contour radius on the energy release rate in the γ–β bicrystal (●), single-phase γ (×) and single-phase β (+): (—) $-1/L$ ($\mathrm{d}E/\mathrm{d}a$), (– –) F_1, Equation 8.

It should be noted that since the E^i calculated using the EAM approach includes both the strain energy (due to lattice distortions) and surface energy (due to a smaller co-ordination number for the atoms near the surface of the crack contributions, the substitution of Equation 12 into Equation 11, yield the net force acting on the crack tip (the F_1 integral) rather than the driving force acting 2γ, where γ is the surface energy of the crack.

To verify the validity of the aforementioned procedure and Equation 12, the F_1 integral was evaluated first for the two single-phase crystals and the results compared with those obtained using Equation 8. As shown in Fig. 9, the two sets of results are in excellent agreement for the case of γ-TiAl in which no phase transformation occurs. For the case of the single-phase β crystal, the agreement is only fair and for the largest contour radius used (18 nm), Equation 12 overestimates F_1 obtained using Equation 8 by about 35%. Nevertheless, it is quite encouraging that the trend in F_1 evaluated using Equation 12 is correct, i.e. the net force acting on the interface is negative and hence this equation is used to evaluate F_1 for the γ–β bicrystal when the crack tip resides in the interface, Fig. 9.

The results shown in Fig. 9 suggests that the martensitic transformation acts more effectively in opposing the crack propagation (i.e. the net force on the crack tip is more negative) when the crack resides in the β-phase as opposed to the case when the crack is in the γ-phase and its tip is at the γ–β interface. This is consistent with the fact that the crack tip opening is smaller in the γ–β case, Fig. 4, than in the β case, Fig. 7. In the β-phase, Fig. 7, a significant amount of transformation is seen taking place in the crack wake (i.e. behind the crack tip), which assists crack-tip blunting. On the contrary, in the γ–β bicrystal, Fig. 4, the crack wake is situated in the γ-phase, which is brittle and provides little assistance to crack-tip blunting.

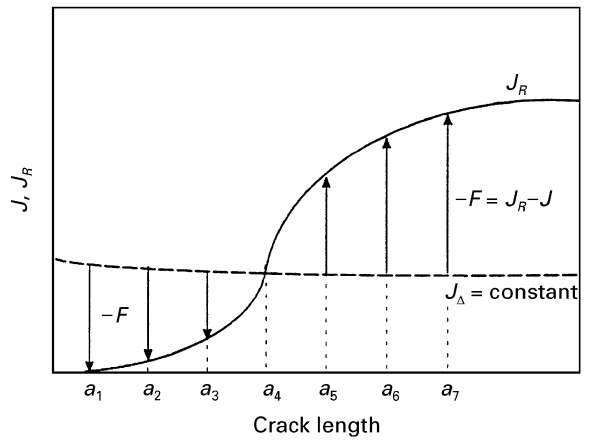

Figure 10 A schematic representation of the fracture resistance, J_R versus a, curve and the fracture driving force, J versus a, curve under constant displacement conditions.

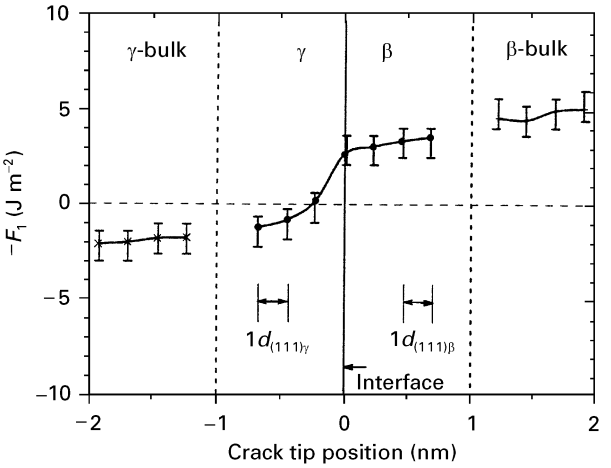

Figure 11 An approximate shape of the fracture resistance curve.

The aforementioned procedure based on the use of Equations 11 and 12 is next employed to obtain a rough estimate of the shape of the fracture resistance (J_R versus a) curve for the case of a crack initially located in the γ-phase that moves into and continues to propagate inside the β-phase. As the schematic shown in Fig. 10 indicates, the shape of the resistance curve is closely related to the $-F_1$ versus a curve under displacement control conditions (Δ = constant).

Fig. 11 shows the $-F_1$ versus a curve obtained using the procedure based on Equations 11 and 12 for the case of a crack in the bulk γ-phase, a crack moving from γ into β and for a crack in the bulk β-phase. All the results shown in Fig. 11 are obtained under the same level of remotely applied uniaxial stress (180 MPa). Error bars are used to indicate the scatter in the $-F_1$ data obtained in each case for a different choice of contour radius. The solid lines are used to connect the data obtained for $R = 15$ nm. The results shown in Fig. 11 suggest that martensitic transformation gives rise to significant enhancement in the toughness of the materials only when the crack tip is located on the β-phase side of the γ–β interface. This implies that the role of martensitic transformation ahead of the crack tip (present also when the crack tip is on the γ-phase side of the γ–β interface) has a less important role in transformation toughening than the transformation taking place in the crack wake behind the crack tip (present only when the crack tip is on the β-phase side of the γ–β interface). This finding is consistent with our previous work in the Fe–Ni system [27], which showed that martensitic transformation in the crack wake plays a critical role in the crack-tip blunting process.

4. Conclusions

Based on the results presented in the present work, the following conclusions can be drawn:

1. When a crack in the γ-TiAl phase makes a contact with the γ-Ti–15 at % V interface, the ensuing martensitic transformation in the β-phase causes significant evolution of the material at the crack tip, which has a major effect on subsequent crack behaviour and toughness of the material.
2. The martensitic transformation involves at least two different crystal structures of martensite, a b.c.o. structure closely related to the h.c.p. structure and an f.c.o. structure, each present in a number of crystallographically equivalent variants. A lattice invariant slip deformation, which accommodates the b.c.c. → f.c.o. transformation shape change, is found to take place in the f.c.o. martensite, while a similar shape change associated with the b.c.c. → b.c.o. martensitic transformation appears to be accommodated by simultaneous formation of at least two b.c.o. variants.
3. The occurrence of martensitic transformation in a region surrounding the crack tip reduces the force acting to propagate the crack and consequently, after the transformed region becomes large enough, crack propagation ceases. The effect of martensitic transformation occurring in the crack wake appears to be particularly strong. Consequently, transformation toughening is more pronounced in the case of a crack residing in the β-phase than in the case of a crack residing in the γ-phase with its tip near the γ–β interface.

Acknowledgements

The work presented here has been supported by the National Science Foundation under grants DMR-9317804 and CMS-9531930. The authors are indebted to Drs Bruce A. MacDonald and William A. Spitzig of NSF for continuing interest in the present work. The help of Professor D. Farkas in providing us with the TiAl EAM potentials is greatly appreciated.

References

1. G. B. OLSON and M. COHEN, in "Mechanical properties and phase transformations in engineering materials", edited by S. D. Antolovich, R. O. Ritchie and W. W. Gerberich, (TMS, American Institute of Mining, Metallurgical and Petroleum Engineers, Warrendale, PA, 1986) p. 367.
2. A. G. EVANS and R. M. CANNON, *Acta Metall.* **34** (1986) 761.
3. P. DANG, PhD thesis, Clemson University, SC (1995).

4. C. L. HOM and R. M. McMEEKING, *Int. J. Solids Struct* **26** (1990) 1211.
5. R. M. McMEEKING and A. G. EVANS, *J. Amer. Ceram. Soc.* **65** (1982) 242.
6. R. G. HOAGLAND, M. S. DAW, M. FOILES and M. I. BASKES, *J. Mater. Res.* **5** (1990) 313.
7. R. G. HOAGLAND, M. S. DAW and J. P. HIRTH, *ibid.* **6** (1991) 2565.
8. A. MONCEVICZ, P. C. CLAPP and J. A. RIFKIN, *Mater. Res. Soc. Symp. Proc.* **213** (1991) 209.
9. Z. Z. YU and P. C. CLAPP, *Metall. Trans.* **20A** (1989) 1617.
10. P. C. CLAPP, Y. SHAO and J. A. RIFKIN, *Mater. Res. Soc. Symp. Proc.* **246** (1992) 1.
11. D. KIM, P. C. CLAPP and J. A. RIFKIN, *ibid.* **213** (1991) 249.
12. F. WILLAIME and C. MASSOBIO, *Phys. Rev.* **B43** (1991) 11 653.
13. M. GRUJICIC and P. DANG, *Mater. Sci. Eng.* **A201** (1995) 194.
14. *Idem*, *ibid.* **A205** (1996) 139.
15. *Idem*, *ibid.* **A205** (1996) 153.
16. M. GRUJICIC and P. DANG, *ibid.* **A199** (1995) 173.
17. P. DANG and M. GRUJICIC, *Script. Metall.* **35** (1996) 59.
18. M. GRUJICIC and P. DANG, *J. Mater. Sci.* **32** (1997) in press.
19. M. S. DAW and M. I. BASKES, *Phys. Rev. Lett.* **50** (1983) 1285.
20. *Idem*, *ibid.* **B29** (1984) 6443.
21. D. FARKAS, Private communication.
22. E. S. MACHLIN, *Acta Metall.* **22** (1974) 95.
23. B. SUNDMAN, Private communication.
24. R. A. JOHNSON, *Phys. Rev.* **B39** (1989) 12 554.
25. A. A. MARADUDIN, E. W. MONTROLL, G. H. WEISS and I. P. IPATOVA, in "Solid state physics, edited by H. Ehrenreich, F. Seitz and D. Turnbull, 2nd Edn (Academic Press, New York, 1971).
26. Pearson's Handbook of Crystallographic Data for Intermetallic Phases, vol. 2, edited by P. Villars and L. D. Calvert (American Society for Metals, Metals Park, OH, 1985).
27. M. GRUJICIC and J. DU, *Modelling. Simul. Mater. Sci.* **3** (1995) 811.
28. M. H. YOO, J. ZOU and C. L. FU, *Mater. Sci. Eng.* **A192/193** (1995) 14.
29. B. deCELIS, A. S. ARGON and S. YIP, *J. Appl. Phys.* **54** (1983) 4864.
30. J. M. RIGSBEE and H. I. ARONSON, *Acta Metall.* **27** (1979) 351.
31. H. C. ANDERSEN, *J. Chem. Phys.* **72** (1980) 2348.
32. J. C. WILLIAMS, in "Titanium science and technology", edited by R. I. Jaffee and H. M. Burte (1973) 1433.
33. W. G. BURGERS, *Physica* **1** (1934) 561.
34. T. W. DURIG, P. M. MIDDLETON, G. T. TERLINDE and J. C. WILLIAMS, in "Titanium science and technology", Vol. 3 edited by R. I. Jaffee and H. M. Burte (1973) p. 1503.
35. G. C. SIH and H. LIEBOWITZ, in "Fracture-an advanced treatise", Vol. II. edited by H. Liebowitz (Academic Press, New York, 1968). p. 67.
36. J. D. ESHELBY, *J. Elasticity* **5** (1975) 321.

Received 19 April 1996
and accepted 2 April 1997